Breaking Reciprocity with Space-Time-Coding Digital Metasurfaces

Lei Zhang, Xiao Qing Chen, Rui Wen Shao, Jun Yan Dai, Qiang Cheng, Giuseppe Castaldi, Vincenzo Galdi,* and Tie Jun Cui*

Metasurfaces are artificially engineered ultrathin structures that can finely tailor and control electromagnetic wavefronts. There is currently a strong interest in exploring their capability to lift some fundamental limitations dictated by Lorentz reciprocity, which have strong implications in communication, heat management, and energy harvesting. Time-varying approaches have emerged as attractive alternatives to conventional schemes relying on magnetic or nonlinear materials, but experimental evidence is currently limited to devices such as circulators and antennas. Here, the recently proposed concept of space-time-coding digital metasurfaces is leveraged to break reciprocity. Moreover, it is shown that such nonreciprocal effects can be controlled dynamically. This approach relies on inducing suitable spatiotemporal phase gradients in a programmable way via digital modulation of the metasurface-elements' phase repsonse, which enable anomalous reflections accompanied by frequency conversions. A prototype operating at microwave frequencies is designed and fabricated for proof-of-concept validation. Measured results are in good agreement with theory, hence providing the first experimental evidence of nonreciprocal reflection effects enabled by space-time-modulated digital metasurfaces. The proposed concept and platform set the stage for "on-demand" realization of nonreciprocal effects, in programmable or reconfigurable fashions, which may find several promising applications, including frequency conversion, Doppler frequency illusion, optical isolation, and unidirectional transmission.

During the past 20 years, metamaterials have been attracting a steadily increasing interest in a wide variety of scientific and engineering disciplines. Metamaterials are artificially engineered structures made of subwavelength inclusions in a host medium, which can manipulate electromagnetic (EM) waves in unconventional ways, and have enabled many exotic physical phenomena and effects, also inspiring novel devices and engineering applications.[1] Their 2D versions, commonly referred to as metasurfaces, are experiencing a strong surge of interest owing to a number of attractive features, including ultrathin thickness, low loss, easy fabrication, and potential conformability. In the wake of the pioneering work by Yu et al.[2] on generalized Snell's laws enabled by imparting an abrupt phase shift, metasurfaces have demonstrated unprecedented capabilities in wavefront engineering, amplitude modulation, and polarization conversion, just to mention a few.[2–6] However, metasurfaces that only impart space-gradient phase discontinuities are inherently constrained by Lorentz reciprocity. This implies, for instance, that the time-reversed version of a reflected wave propagates along the same direction as the original incident wave at the same frequency.

The quest for breaking reciprocity is of longstanding interest in EM engineering, and is currently eliciting renewed attention in view of its pivotal role in lifting some fundamental limitations in communication systems as well as energy harvesting and heat management.[7–24] For instance, in wireless communication systems, a nonreciprocal antenna could radiate a very directive beam without being bound to receiving its reflected echo.[20] A common way to attain nonreciprocal effects, especially at microwave frequencies, is to break the time-reversal symmetry by means of biased magnetic materials (e.g., ferrites). These, however, are typically bulky, costly, and difficult to integrate and scale up to optical wavelengths,[10] which motivates the strong interest in magnetless approaches. Some of these are based on nonlinear materials, which are not bound by the reciprocity theorem, but are power-dependent and require sufficiently high signal intensity.[11,12] Other magnetless approaches rely on transistor-based devices[13] and moving media,[14,15] but are limited in terms of operating frequency, and are difficult to extend to the optical regime. Time-varying approaches have emerged as attractive alternatives based on time-modulated devices,[16–24] which have smaller size, lower cost, and better integrability. In 2015, Shaltout et al.[19]

L. Zhang, X. Q. Chen, R. W. Shao, J. Y. Dai, Prof. Q. Cheng, Prof. T. J. Cui
State Key Laboratory of Millimeter Waves
Southeast University
Nanjing 210096, China
E-mail: tjcui@seu.edu.cn
Prof. G. Castaldi, Prof. V. Galdi
Fields & Waves Lab
Department of Engineering
University of Sannio
I-82100 Benevento, Italy
E-mail: vgaldi@unisannio.it

The ORCID identification number(s) for the author(s) of this article can be found under https://doi.org/10.1002/adma.201904069.

introduced time-gradient phase discontinuities in time-varying metasurfaces to control the normal momentum component, thereby breaking the time-reversal symmetry and Lorentz reciprocity. In the same year, Hadad et al.[18] demonstrated a non-reciprocal electromagnetic-induced-transparency phenomenon enabled by a space-time gradient metasurface, by adding transverse temporal modulation to the electronic properties of the surface impedance. The time-varying route to nonreciprocity has been successfully validated for devices such as circulators[17] and antennas,[20] but the inherent difficulties in imparting a continuous space-time modulation in the surface impedance have so far hindered an experimental demonstration of nonreciprocal metasurfaces based on this principle. This motivates our study here, which relies on space-time-coding digital metasurfaces.

The concept of digital coding and programmable metasurfaces was originally proposed by Cui et al. in 2014,[25] and has been rapidly developed and implemented in many applications.[25–40] Such metasurfaces are composed of a limited numbers of meta-atoms and can control EM waves in a discretized manner, which offers the inherent advantage of greatly simplifying the design and optimization procedures. For example, an n-bit coding metasurface typically consists of 2^n distinct elements with reflection/transmission phases varying in discrete steps of $2\pi/2^n$. The digital representation of coding metasurfaces is remarkably suitable for integrating active devices (e.g., diodes), which can be independently controlled by a field- programmable gate array (FPGA), thereby leading to programmable metasurfaces. These concepts have been widely explored in several applications including holograms,[26] imaging,[27] vortex beams,[28,40] reflect and transmit arrays,[29–32] diffuse scattering,[33,34,40] information processing,[35,36] and new architectures of wireless communication systems.[37–39] More recently, a general theory of space-time-coding digital metasurfaces has been proposed[40] to enable simultaneous manipulations of EM waves in both the space and frequency domains, such as harmonic beam steering.

In this work, by judiciously designing 2-bit space and time-gradient coding sequences, we leverage this concept to break the time-reversal symmetry in two-port reflection systems, so as to obtain nonreciprocal reflection and frequency conversion. First, we outline the basic theory of nonreciprocal space-time-coding digital metasurfaces. Subsequently, we present several examples to demonstrate nonreciprocal effects in both the space and frequency domains. Finally, we fabricate and test a prototype for experimental validation at microwave frequencies. The proposed approach also allows dynamic control of the non-reciprocal effects, and is expected to find potential applications to a wide variety of nonreciprocal systems.

We consider a 2D scenario featuring a reflecting digital programmable metasurface composed by N columns of elements, whose reflection-coefficient phase is controlled via switching elements such as positive-intrinsic-negative (PIN) diodes activated by a digital code. The structure is obliquely illuminated by a time-harmonic plane wave with suppressed time-dependence $exp(j2\pi f_c t_c)$, transverse-magnetic polarization (i.e., out-of-plane magnetic field), and incidence angle θ_i. The generic pth coding element is subject to a time modulation of the reflection coefficient, assumed as a periodic function $\Gamma_p(t) = \sum_{n=1,...,L} \Gamma_p^n U_p^n(t)$, with $U_p^n(t)$ denoting a periodic impulse function with modula-

tion period T_0.[40] Therefore, each element is characterized by a time-coding sequence of length L, and the entire structure can be compactly represented in terms of a space-time-coding matrix.[40] According to our previously developed theory of space-time-coding metasurfaces,[40] for modulation frequencies $f_0 = 1/T_0$ much smaller than the plane-wave frequency f_c, the time-domain scattered far-field can be expressed approximately as

$$f(\theta,t) = \sum_{p=1}^N E_p(\theta)\Gamma_p(t)\exp\left[j\frac{2\pi}{\lambda_c}(p-1)d(\sin\theta + \sin\theta_i) \right] \quad (1)$$

where $E_p(\theta) = \cos\theta$ is the scattering pattern (approximated by a cosine function) of the pth coding element at the center operational frequency f_c, $\lambda_c = c/f_c$ is the center operational wavelength (with c denoting the speed of light in vacuum), and d is the period of the coding elements. By Fourier-series expansion of the reflection coefficient $\Gamma_p(t)$, the scattered far-field at the mth harmonic frequency $f_c + mf_0$ can be written as

$$F_m(\theta) = \sum_{p=1}^N E_p(\theta)a_p^m\exp\left[j2\pi(p-1)d\left(\frac{\sin\theta}{\lambda_r} + \frac{\sin\theta_i}{\lambda_c}\right) \right] \quad (2)$$

where $\lambda_r = c/(f_c + mf_0)$ is the wavelength of the reflected waves corresponding to the mth harmonic frequency, and a_p^m are the Fourier coefficients of $\Gamma_p(t)$, given by[40]

$$a_p^m = \sum_{n=1}^L \frac{\Gamma_p^n \sin(\pi m/L)}{\pi m} exp[-j\pi m(2n-1)/L] \quad (3)$$

Figure 1 schematically illustrates the nonreciprocal effects[19] that we are interested in engineering via the above approach. Specifically, we aim at designing the space-time coding so that a plane wave impinging at an angle θ_1 and frequency f_1 is anomalously reflected at an angle θ_2 and frequency f_2. For the time-reversal scenario, however, an incident plane wave with angle θ_2 at frequency f_2 is reflected at an angle $\theta_3 \neq \theta_1$ and frequency $f_3 \neq f_1$. This clearly breaks the time-reversal symmetry, and hence Lorentz reciprocity.[19]

To this aim, we consider a space-time-coding metasurface made of 16 space-coding elements with periodic time-coding sequences of length $L = 4$, compactly represented via the space-time-coding matrix in **Figure 2**a. Basically, each coding element is subject to a temporal phase gradient with steps of 90°, and the temporal sequences across the structure are progressively shifted by an interval $T_0/4$ so that, in every modulation interval, two adjacent metasurface elements exhibit a 90° phase difference. This simple 2-bit space-time-coding establishes a spatiotemporal phase gradient distribution which mainly converts an incident plane wave at the center operational frequency f_c into the +1st harmonic frequency $f_c + f_0$, as demonstrated by the equivalent amplitudes in Figure 2b [obtained via Equation (3)]. Moreover, the equivalent phases in Figure 2c exhibit a phase gradient at the +1st harmonic frequency, which steers the reflected wave toward a specific direction. Accordingly, the calculated spectrum distribution in Figure 2d indicates that the incident wave is mainly converted into the +1st harmonic frequency with a reflection amplitude of 0.9. It should be mentioned that the scheme is rather robust with respect to possible imperfections in the phase responses of the coding elements.
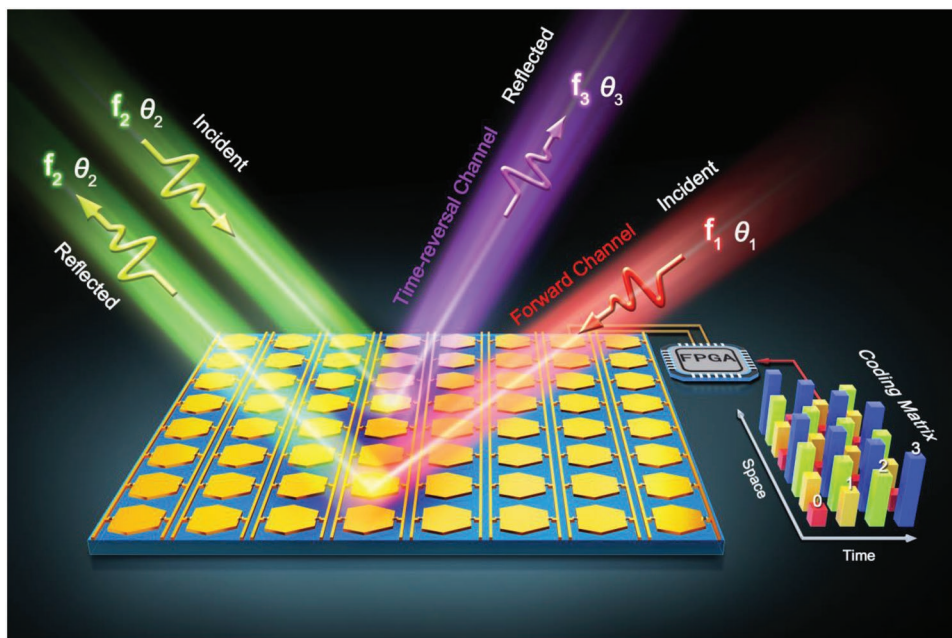
**ADVANCED
SCIENCE NEWS**
www.advancedsciencenews.com

**ADVANCED
MATERIALS**
www.advmat.de

Figure 1. Conceptual illustration of the nonreciprocal reflection based on a space-time-coding metasurface. Schematics of the forward and time-reversal reflection scenarios.

As an example, Figure 2d also shows (green bars) the results obtained by assuming an imperfect phase distribution, with phase steps among adjacent 2-bit coding states not exactly of 90°. As it can be observed, these results are very similar to those (red bars) pertaining to the ideal 90°-step phase distribution, with the appearance of weakly excited spurious harmonics.

Recalling that the time-coding sequence of the generic pth element in Figure 2a is derived from the periodic function $\Gamma_p(t)$ by applying a time shift $t_p = (p-1)T_0/4$, from basic Fourier-series theory,[40] it follows that the phase difference $\Delta\psi_m$ between adjacent coding elements at the mth harmonic frequency $f_c + mf_0$ can be written as

$$\Delta\psi_m = -2\pi mf_0(t_{p+1} - t_p) = -\frac{m\pi}{2} \tag{4}$$

Therefore, the effective space-gradient phase shift for the +1st harmonic frequency is given by

$$\frac{\partial\psi}{\partial x} = \frac{\Delta\psi_1}{d} = -\frac{\pi}{2d} \tag{5}$$

Recalling the forward-incidence scenario in Figure 1, for an incident plane wave with frequency f_c and wavenumber $k = 2\pi f_c/c$, the dominant reflected order is at frequency $f_c + f_0$ and wavenumber $k + \Delta k = 2\pi(f_c + f_0)/c$. The relationship between the incidence (θ_1) and reflection (θ_2) angles is given by[19]

$$(k + \Delta k)\sin\theta_2 = k\sin\theta_1 + \frac{\partial\psi}{\partial x} \tag{6}$$

For the time-reversal scenario in Figure 1, by assuming an incident wave with frequency $f_c + f_0$ and wavenumber $k + \Delta k = 2\pi(f_c + f_0)/c$, the dominant reflected order is now at frequency

$f_c + 2f_0$ and wavenumber $k + 2\Delta k = 2\pi(f_c + 2f_0)/c$, and the relationship between the incidence (θ_2) and reflection (θ_3) angles becomes[19]

$$(k + 2\Delta k)\sin\theta_3 = (k + \Delta k)\sin\theta_2 - \frac{\partial\psi}{\partial x} \tag{7}$$

After straightforward algebra from Equations (6) and (7), the reflection angles in the forward and time-reversal scenarios (θ_2 and θ_3, respectively) are found to satisfy the following relationships

$$\sin\theta_2 = \frac{k\sin\theta_1 + \frac{\partial\psi}{\partial x}}{k + \Delta k} = \frac{\sin\theta_1 - \frac{\lambda_c}{4d}}{1 + \frac{f_0}{f_c}} \tag{8}$$

$$\sin\theta_3 = \frac{k}{k + 2\Delta k}\sin\theta_1 = \frac{\sin\theta_1}{1 + \frac{2f_0}{f_c}} \tag{9}$$

To quantify the angular separation between the time-reversed reflected and incident waves, we define a deviation factor

$$\delta = |\sin\theta_3 - \sin\theta_1| = \frac{\sin\theta_1}{1 + \frac{f_c}{2f_0}} \tag{10}$$

which is always nonzero for oblique incidence. To sum up, the reflected wave in the time-reversal scenario does not propagate along the same direction as the original obliquely incident wave, and is also accompanied by a frequency shift of $2f_0$, thereby clearly breaking the time-reversal symmetry and Lorentz reciprocity in both the space and frequency domains. Equation (10)
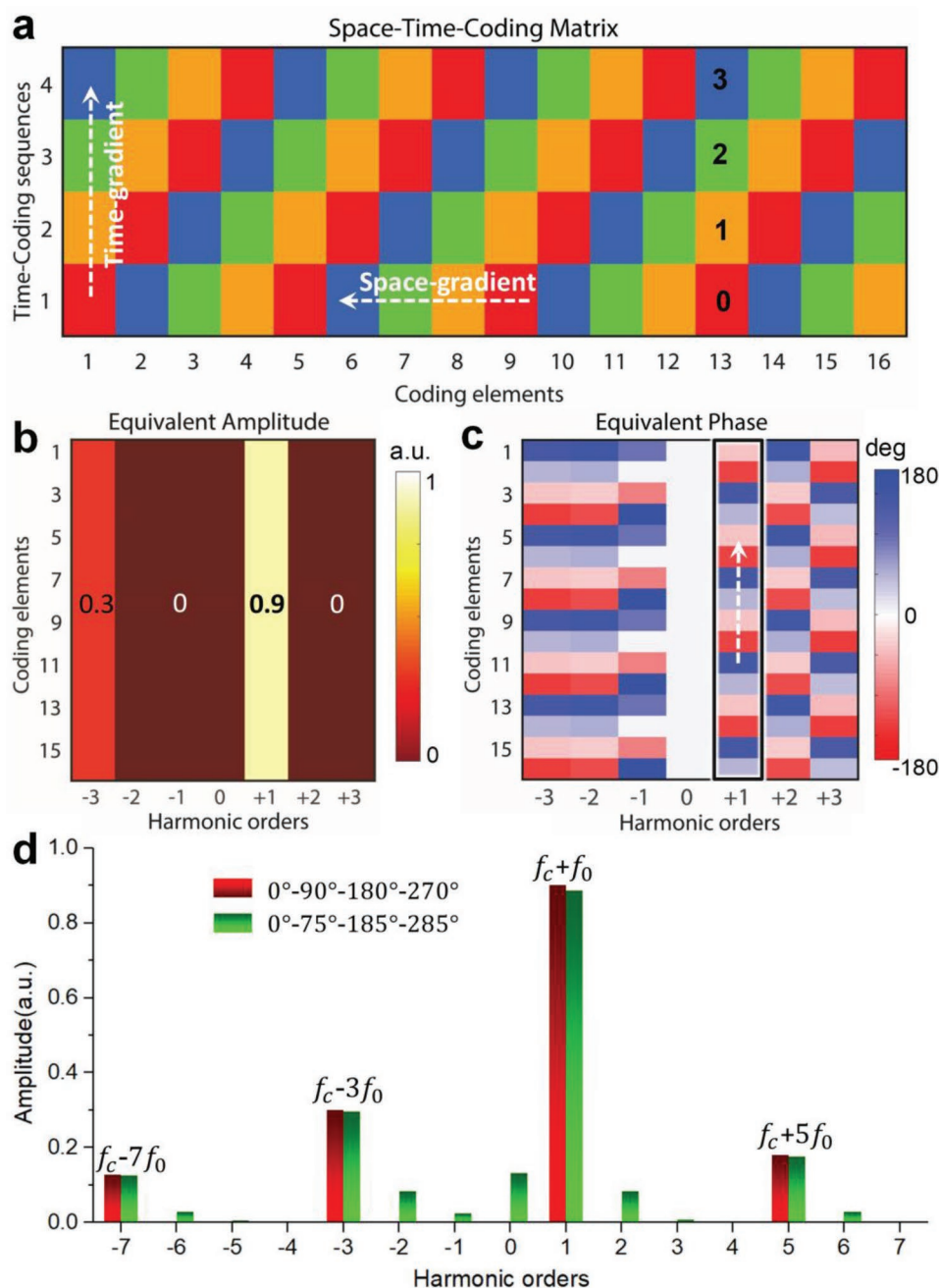
Figure 2. Space-time-coding matrix for realizing nonreciprocal reflection. a) 2D space-time-coding matrix of dimension 16 × 4, in which the red, yellow, green, and blue squares represent the "0," "1," "2," and "3" digits, respectively. Adjacent digits correspond to coding elements characterized by a 90° phase difference. b,c) Equivalent amplitude and phase distributions, respectively, for the coding elements at different harmonic frequencies. d) Corresponding theoretical predictions for the spectral distributions of the harmonic orders (red bars). Also shown (green bars), as a reference, are the corresponding values pertaining to an imperfect phase distribution with steps not exactly of 90°.

indicates that the angular separation increases with the ratio f_0/f_c and the incidence angle θ_1. If the modulation frequency f_0 is exceedingly smaller than the center operational frequency f_c, this spatial separation may be impossible to observe in practical experiments. Nevertheless, by suitably increasing the frequency ratio f_0/f_c and the incidence angle θ_1, the angular separation may become on the order of few degrees (see Figure S1, Supporting Information). It should also be mentioned that

the nonreciprocal effect can be realized only in the frequency domain when the space-time-coding metasurface is illuminated by a normally incident wave ($\theta_1 = 0°$) in the forward scenario. In this case, the reflection angle θ_3 in the time-reversal scenarios is $\theta_3 = \theta_1 = 0°$, and hence there is no spatial separation between the time-reversed reflected and incident waves.

We start by assuming $f_c = 5$ GHz, $f_0 = 250$ MHz, $d = \lambda_c/2$, and $\theta_1 = 60°$. In this case, the reflection angles in forward and

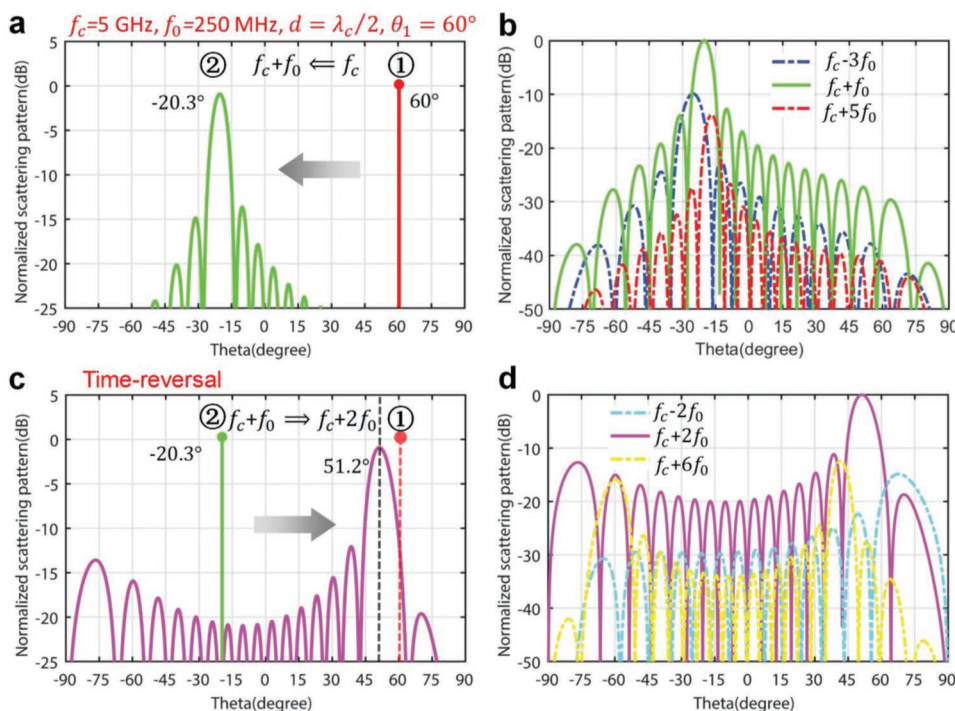**Figure 3.** Numerical example, assuming $f_c = 5$ GHz, $f_0 = 250$ MHz, $d = \lambda_c/2$, and $\theta_1 = 60°$. a,b) Scattering patterns in the forward scenario (excitation from Port 1 at f_c and $\theta_i = 60°$). c,d) Scattering patterns in the time-reversal scenario (excitation from Port 2 at $f_c + f_0$ and $\theta_i = 20.3°$). Note that, in (a) and (b), negative values of the observation angle indicate positive values of the reflection angle; in (c) and (d), the incidence angle is expressed in negative values. For better visibility, (a) and (c) show the dominant order only, whereas (b) and (d) compare the three dominant orders.

time-reversal scenarios (at frequencies $f_c + f_0$ and $f_c + 2f_0$, respectively) are theoretically predicted as $\theta_2 = 20.40°$ and $\theta_3 = 51.93°$, respectively, with the corresponding scattering patterns shown in **Figure 3**. More specifically, referring to the forward scenario in Figure 1, with the plane wave impinging obliquely at an angle of 60° and frequency f_c (from Port 1), the scattering patterns at the various harmonic frequencies are shown in Figure 3a,b. It can be observed that the dominant beam occurs at frequency $f_c + f_0$ and points at an angle of $-20.3°$ (Port 2), with its maximum power ≈10 dB higher than those at other harmonic frequencies. Therefore, the incident wave at an angle $\theta_1 = 60°$ and frequency f_c is mainly converted into a reflected wave at an angle $\theta_2 = 20.3°$ and frequency $f_c + f_0$. Considering now the time-reversal case in Figure 1, with the plane wave now impinging at an angle $\theta_2 = 20.3°$ and frequency $f_c + f_0$ (i.e., from Port 2), the dominant reflected beam occurs instead at frequency $f_c + 2f_0$ and points at an angle $\theta_3 = 51.2°$ (Port 3), as shown in Figure 3c,d. The beam angles θ_2 and θ_3 in the scattering patterns are in good agreement with the theoretical predictions via Equations (8) and (9). For this parameter configuration, the angle of the time-reversed reflected wave θ_3 is quite different from the incidence angle θ_1, and the reflected beam also experiences a frequency shift of $2f_0$ with respect to the incident wave. This nonreciprocal-reflection effect can be exploited to isolate the wave transmission in both the space and frequency domains. Thus, for instance, the space-time-coding digital metasurface can be used as an isolator with two ports placed along the directions of the incident (θ_1) and reflected (θ_2) waves; the transmission is enabled from Port 1 to Port 2, but

it is suppressed (due to the angular separation and frequency shift) from Port 2 to Port 1.

With a view toward a practical design in the X-band ($f_c = 9.5$ GHz), we note that in order to attain angular separations that are experimentally observable, the modulation frequency f_0 should be at least 500 MHz. According to the time-coding sequence in Figure 2a, the switching speed of the PIN diodes should be $4f_0 = 2$ GHz (i.e., switching time of 0.5 ns), which is not feasible with currently available commercial PIN diodes. Although, in principle, these limitations could be overcome by lowering the center operational frequency, this is inherently limited by the size and operability of our experimental facility, as it would entail working with larger metasurfaces (in order to attain reflected beams with appropriate beamwidths), larger antenna–metasurface distances (in order to obtain reasonably planar incident wavefronts), and poorer absorption properties of the anechoic chamber. Even considering the lowest frequency (2 GHz) compatible with the size of our experimental facility (entailing a metasurface size of ≈1.2 × 0.6 m² and an antenna–metasurface distance of ≈2 m), the required switching speed would still beyond reach for currently available commercial PIN diodes. Therefore, we did not find this option practically viable. Finally, it should also be mentioned that, in our operational regime, increasing the value of the incidence angle is not an effective option, as for modulation frequencies much smaller than the center operational frequency it has little effect in the angular separation (see Figure S1, Supporting Information). In the future, we plan to explore alternative modulation schemes based on graphene, for which modulation frequencies
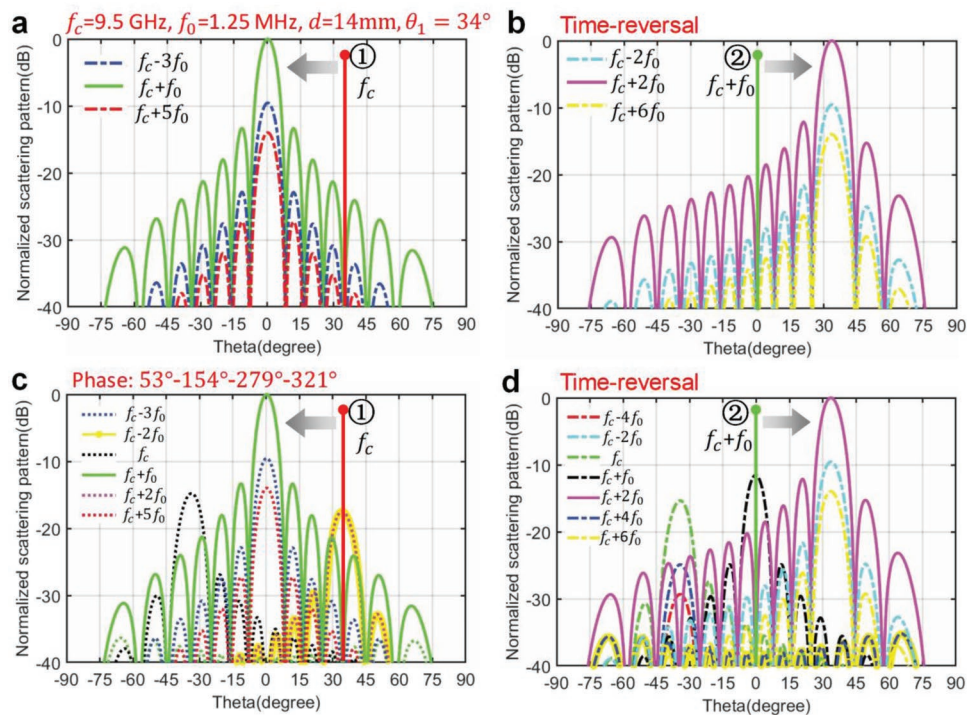
**ADVANCED
SCIENCE NEWS**

www.advancedsciencenews.com

**ADVANCED
MATERIALS**

www.advmat.de

Figure 4. Numerical example corresponding to the experimental realization, assuming f_c = 9.5 GHz, f_0 = 1.25 MHz, d = 14 mm, and θ_1 = 34°. a) Scattering patterns in the forward scenario (excitation from Port 1 at f_c and θ_i = 34°). b) Scattering pattern in the time-reversal scenario (excitation from Port 2 at $f_c + f_0$ and θ_i = 0°). c,d) As in (a) and (b), respectively, but assuming an imperfect phase distribution in the 2-bit coding elements (namely, 53°, 154°, 279°, and 321°), that is, with phase steps not exactly of 90°.

over tens of GHz have been demonstrated.[21] For our current implementation relying on PIN diodes, it is difficult to observe the nonreciprocal effects in the space domain, but it is still possible to observe them in the frequency domain by means of a high-precision spectrum analyzer. Specifically, we assume f_c = 9.5 GHz, f_0 = 1.25 MHz, d = 14 mm, and θ_1 = 34°. Along the same lines of the previous example, **Figure 4**a,b shows the scattering patterns pertaining to the forward and time-reversal scenarios, respectively. In the forward case, it can be observed that the dominant reflected beam is at frequency $f_c + f_0$ = 9.50125 GHz and angle θ_2 = 0.27° whereas, in the time-reversal scenario, the dominant reflected beam is at frequency $f_c + 2f_0$ = 9.5025 GHz and angle θ_3 = 33.7°, and the center-frequency component at f_c = 9.5 GHz disappears. Although the very small angular separation ($\theta_3 - \theta_1$) prevents a clear observation of the phenomenon in the space domain, nonreciprocity can be demonstrated in terms of frequency isolation, by considering different frequency ports.

We further study the robustness of the nonreciprocal effects when the phase step in adjacent 2-bit coding states is not exactly 90°, in view of the inevitable imperfections in the design and practical experiments (see Figure S2, Supporting Information). As an example, Figure 4c,d shows the results pertaining to the same scenarios as in Figure 4a,b, respectively, but now assuming as the reflection-coefficient phases of the 2-bit coding elements: 53°, 154°, 279°, and 321°. We observe that the phase imperfections yield some new harmonic components, but the desired frequency components still dominate in both the forward and time-reversal scenarios, thereby

indicating a general robustness of the nonreciprocal reflection phenomenon.

To experimentally validate the above concepts and nonreciprocal effects, we design a 2-bit space-time-coding digital metasurface composed of 16 × 8 coding elements to implement the configuration in Figure 4. As shown in **Figure 5**a, each column of the metasurface is composed of eight coding elements and shares a common control voltage. Each coding element consists of a hexagonal metal patch and two biasing lines printed on a grounded F4B substrate with dielectric constant 2.65, loss tangent 0.001, and thickness 1.5 mm. Two PIN diodes (M/A-COM MADP-000907-14020x) are employed to connect the hexagonal patch with two biasing lines, as illustrated in Figure 5b. The size of the coding element is 14 × 14 mm², corresponding to about $0.44\lambda_c \times 0.44\lambda_c$ at the center operational frequency of 9.5 GHz. The parameters of the coding elements are engineered so as to attain a 90° phase difference when two PIN diodes switch among "OFF-OFF," "ON-OFF," "OFF-ON," and "ON-ON" states (see the Supporting Information), corresponding to the four coding states "0," "1," "2," and "3," respectively. Full-wave simulations are carried out by means of the commercial software package CST Microwave Studio 2014 (www.cst.com/products/cstmws). In simulating the response of the coding elements, periodic boundary conditions are applied along the x and y-directions, and two Floquet ports are used along the $+z$ and $-z$-directions. A normally incident plane-wave illumination with x-polarized electric field is assumed to calculate the reflection coefficients. The phase and amplitude responses pertaining to the four coding states "0," "1," "2," and "3" are

**ADVANCED
SCIENCE NEWS**
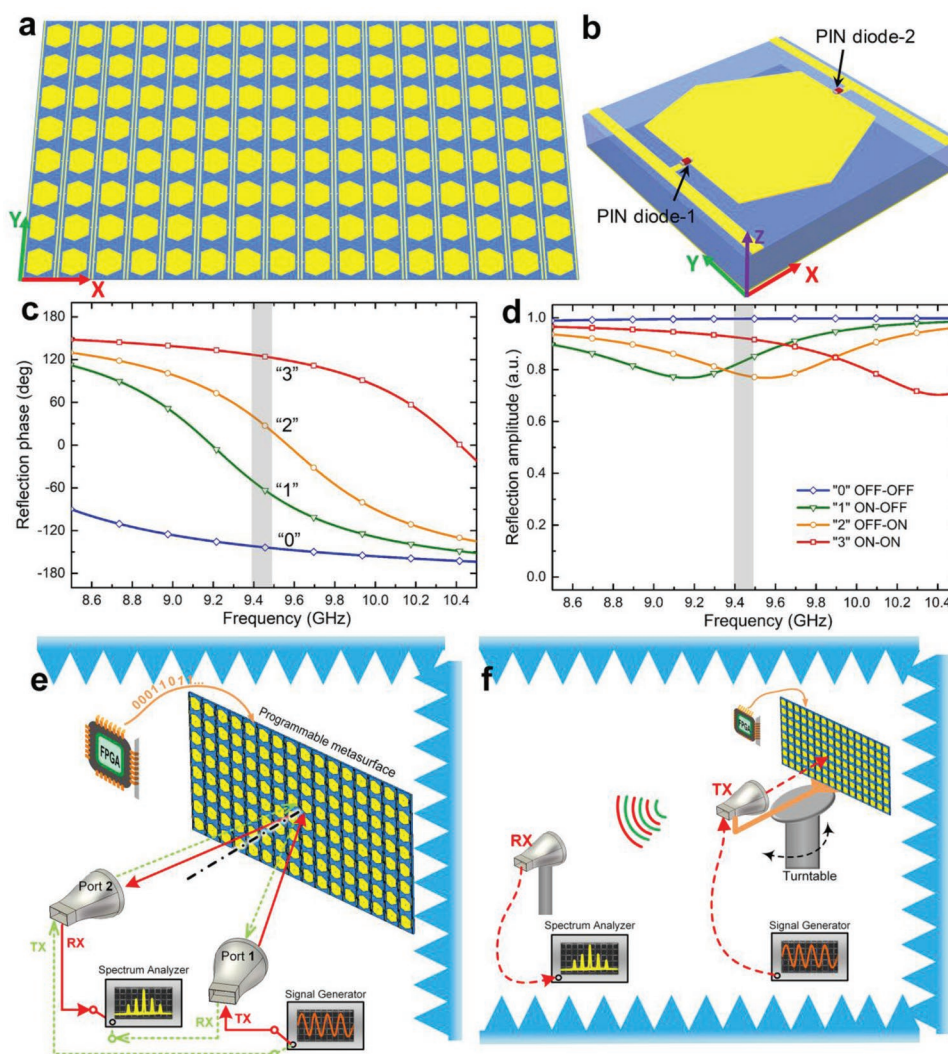www.advancedsciencenews.com

**ADVANCED
MATERIALS**
www.advmat.de

Figure 5. Prototype design and schematic of experimental setups. a) Schematic view of the realized 2-bit space-time-coding digital metasurface prototype 16×8 coding elements. b) Geometry of the 2-bit programmable coding element loaded with two PIN diodes. c,d) Numerically computed reflection-coefficient phase and amplitude responses, respectively, of the 2-bit coding element excited by a normally incident plane wave (with x-polarized electric field), for the four possible combinations of the diodes states. The gray-shaded areas delimit a neighborhood of the chosen operational frequency. e,f) Schematics of the experimental setups for measuring the scattered spectral power distribution and the far-field scattering patterns, respectively, for the forward and time-reversal scenarios.

shown in Figure 5c,d, respectively. We observe that the phase difference between adjacent 2-bit coding states is ≈90° at the frequency of 9.5 GHz, and the corresponding amplitudes exceed 0.79. It is worth mentioning that, although the structure is designed by assuming normal incidence, the experimental validation also implies operation under oblique incidence. The angular stability of the design is discussed in detail in the Supporting Information.

Based on the above design, we fabricate a prototype of the proposed metasurface, as shown in **Figure 6**b. The structure consists of 16 columns with eight connected elements, and has an overall size of 224×123 mm^2 ($7.1\lambda_c \times 3.9\lambda_c$). The experiments are carried out in a microwave anechoic chamber, as illustrated in Figure 6a. In this experiment, the assumptions are the same as in the example in Figure 4. The fabricated prototype is first illuminated by the transmitting (TX) horn antenna

placed along the direction $\theta_1 = 34°$ (Port 1) with the excitation signal at 9.5 GHz. Figure 6c shows the scattering patterns pertaining to the forward scenario, with a dominant reflected beam at 9.50125 GHz and an angle of ≈0°. For the time-reversal scenario, that is, when the prototype is illuminated by the TX horn antenna placed along the direction $\theta_2 = 0$ (Port 2) with the excitation signal at 9.50125 GHz, the scattering patterns are shown in Figure 6d, with a dominant reflected beam at 9.50250 GHz and an angle of ≈ 34°. It should be mentioned that the phases of the 2-bit coding elements measured via a vector network analyzer (Keysight N5230C) are consistent with those considered in Figure 4c,d, which are not exactly in steps of 90° due to the unavoidable design imperfections, modeling uncertainties, and fabrication tolerances. Nevertheless, we can clearly observe that the reflection angles and harmonic distributions of the measured scattering patterns are in good agreement with
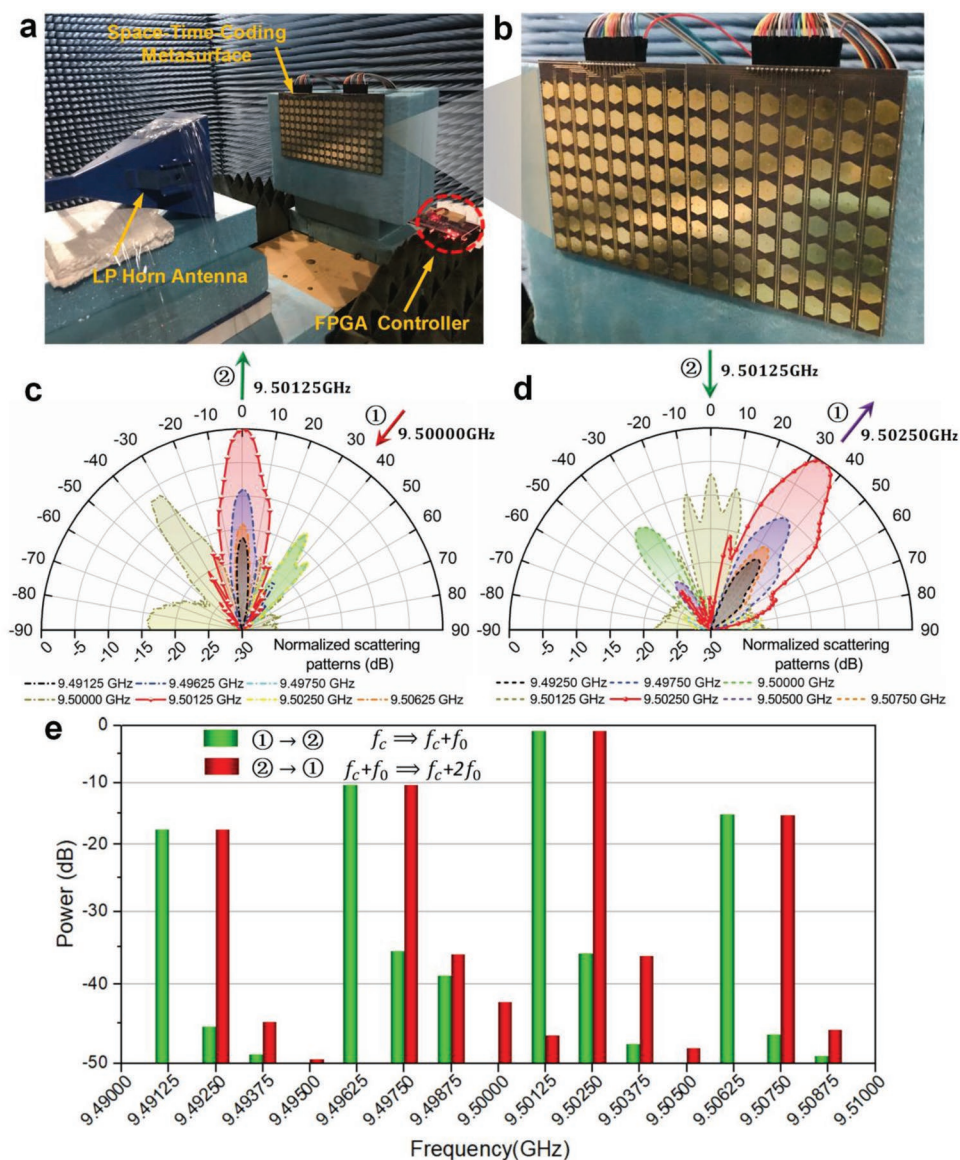
**ADVANCED
SCIENCE NEWS**

www.advancedsciencenews.com

**ADVANCED
MATERIALS**

www.advmat.de

Figure 6. Experimental setup and results. a,b) Photographs of the experimental setup in an anechoic chamber and the fabricated prototype, respectively. c,d) Measured scattering patterns at different harmonic frequencies, for the forward and time-reversal scenarios, respectively. e) Comparison between measured spectral power distributions pertaining to the forward (green bars) and time-reversal (red bars) scenarios.

the theoretical predictions in Figure 4c,d, thereby validating the proposed approach.

As anticipated, due to the small angle separation between the directions of time-reversal reflected and incident waves, it is difficult with our experimental setup to resolve these contributions in the space domain. Nevertheless, the nonreciprocal effects are clearly observed in the frequency domain, by examining the spectrum power distribution via the measurement setup in Figure 5e. As shown in Figure 6e (green bars), for the forward scenario, an incident wave at frequency of 9.5 GHz transmitted from Port 1 is mainly converted into a reflected beam at frequency of 9.50125 GHz received at Port 2. Conversely, in the time-reversal scenario (with the transmitting and receiving (RX) ports in Figure 5e interchanged), a wave at frequency of 9.50125 GHz transmitted from Port 2 is mainly converted

into a reflected beam at frequency of 9.50250 GHz received at Port 1, as illustrated in Figure 6e (red bars). This frequency is different from that of the wave transmitted wave from Port 1 (9.5 GHz) in the forward scenario, thereby providing experimental evidence of nonreciprocity in the frequency domain. Additional results on the measured spectra are discussed in the Supporting Information.

It should also be mentioned that, when the FPGA controller provides time-invariant space coding sequences, the metasurface exhibits a reciprocal response (see Figure S4b,c, Supporting Information). Therefore, we can simply switch between the states of nonreciprocity and reciprocity by changing the codes stored in the FPGA. Furthermore, the frequency shifts of the time-reversed reflected wave can be programmed by changing the optimized space-time-coding matrix preloaded

in the FPGA. In other words, our proposed FPGA-controlled space-time-coding metasurface can realize "programmable" nonreciprocal and/or reciprocal effects in the frequency domain (see the Supporting Information), which is very promising for designing novel functionalities in future isolators and mixers.

In summary, we have proposed a 2-bit space-time-coding digital metasurface which can break Lorentz reciprocity, and can isolate the wave reflections in both the space and frequency domains. By suitably designing the space-time coding sequences, we have demonstrated that the metasurface sustains a spatiotemporal phase gradient that breaks the time-reversal symmetry and induces nonreciprocal wave reflections. Specifically, the time-reversed reflected wave does not propagate along the same direction of the incident wave, and also experiences a frequency shift. Finally, we have fabricated and experimentally characterized at microwave frequencies an FPGA-controlled prototype to validate the proposed approach. The obtained results, in good agreement with the theoretical predictions, provide the first experimental evidence of nonreciprocal reflection effects enabled by space-time-modulated metasurfaces. The current implementation and experimental setup only allowed a demonstration in the frequency domain, since the angular separation between the time-reversed-reflected and incident waves was too small (<1°) to be resolved. In future studies, we plan to increase the angular separation up to measurable values by exploring different implementations such as graphene-based or femtosecond laser-driven, which should allow substantially higher modulation frequencies and could also be extended to the terahertz and possibly optical regimes.

Overall, our proposed concept and platform significantly enrich the wave-manipulation capabilities of digital metasurfaces, by enabling the "on-demand" realization of nonreciprocal effects in a completely programmable (via FPGA) and reconfigurable fashion. This brings about new dimensionalities in the grand vision of "software-defined" and "cognitive" metamaterials,[35] and may find important applications to isolator, mixer, duplexer, frequency conversion, Doppler frequency illusion, unidirectional transmission, as well as nonreciprocal wireless and radar systems with separated transmitting and receiving channels.

Experimental Section

The schematics of the setup for measuring the spectrum distributions and far-field scattering patterns are shown in Figure 5e,f, respectively. For measuring the spectral power distributions, two linearly polarized horn antennas working from 8 to 12 GHz were placed at the predesigned directions of Ports 1 and 2, and were alternated as TX and RX antennas for the forward and time-reversal scenarios, respectively. The TX horn antenna was connected to a microwave signal generator (Keysight E8257D), while the RX horn was connected to a spectrum analyzer (Keysight E4447A), as illustrated in Figure 5e. Figure 5f instead illustrates the setup for measuring the far-field scattering patterns. In this case, both the metasurface and TX horn antenna were mounted on a turntable, which can be rotated automatically by 360° in the horizontal plane. The RX horn antenna was used to receive the scattered harmonic signals via the spectrum analyzer. To provide dynamic biasing voltages for the 2-bit digital metasurface, an FPGA hardware control board was exploited, in which a computer code is preloaded to generate 32 control voltages based on the space-time-coding matrix in Figure 2a. The modulation frequency f_0 is 1.25 MHz, corresponding to a switching speed of 5 MHz for the PIN diodes.

Supporting Information

Supporting Information is available from the Wiley Online Library or from the author.

Conflict of Interest

The authors declare no conflict of interest.

[1] N. I. Zheludev, Y. S. Kivshar, *Nat. Mater.* **2012**, *11*, 917.

[2] N. F. Yu, P. Genevet, M. A. Kats, F. Aieta, J. P. Tetienne, F. Capasso, Z. Gaburro, *Science* **2011**, *334*, 333.

[3] C. L. Holloway, E. F. Kuester, J. A. Gordon, J. O'Hara, J. Booth, D. R. Smith, *IEEE Antennas Propag. Mag.* **2012**, *54*, 10.

[4] N. M. Estakhri, A. Alù, *J. Opt. Soc. Am. B* **2015**, *33*, A21.

[5] A. V. Kildishev, A. Boltasseva, V. M. Shalaev, *Science* **2013**, *339*, 1232009.

[6] N. K. Grady, J. E. Heyes, D. R. Chowdhury, Y. Zeng, M. T. Reiten, A. K. Azad, A. J. Taylor, D. A. Dalvit, H. T. Chen, *Science* **2013**, *340*, 1304.

[7] S. H. Fan, Y. Shi, Q. Lin, *IEEE Antennas Wireless Propag. Lett.* **2018**, *17*, 1948.

[8] C. Caloz, A. Alù, S. Tretyakov, D. Sounas, K. Achouri, Z.-L. Deck-Léger, *Phys. Rev. Appl.* **2018**, *10*, 047001.

[9] E. Verhagen, A. Alù, *Nat. Phys.* **2017**, *13*, 922.

[10] J. D. Adam, L. E. Davis, G. F. Dionne, E. F. Schloemann, S. N. Stitzer, *IEEE Trans. Microwave Theory Tech.* **2002**, *50*, 721.

[11] Y. Shi, Z. Yu, S. Fan, *Nat. Photonics* **2015**, *9*, 388.

[12] A. M. Mahmoud, A. R. Davoyan, N. Engheta, *Nat. Commun.* **2015**, *6*, 8359.

[13] S. Taravati, B. A. Khan, S. Gupta, K. Achouri, C. Caloz, *IEEE Trans. Antennas Propag.* **2017**, *65*, 3589.

[14] R. Fleury, D. L. Sounas, C. F. Sieck, M. R. Haberman, A. Alù, *Science* **2014**, *343*, 516.

[15] Y. Mazor, A. Alù, *Phys. Rev. B* **2019**, *99*, 045407.

[16] Z. Yu, S. Fan, *Nat. Photonics* **2009**, *3*, 91.

[17] N. A. Estep, D. L. Sounas, J. Soric, A. Alù, *Nat. Phys.* **2014**, *10*, 923.

[18] Y. Hadad, D. L. Sounas, A. Alù, *Phys. Rev. B* **2015**, *92*, 100304.

[19] A. Shaltout, A. Kildishev, V. Shalaev, *Opt. Mater. Express* **2015**, *5*, 2459.

[20] Y. Hadad, J. C. Soric, A. Alù, *Proc. Natl. Acad. Sci. USA* **2016**, *113*, 3471.

[21] D. Correas-Serrano, J. S. Gomez-Diaz, D. L. Sounas, Y. Hadad, A. Alvarez-Melcon, A. Alù, *IEEE Antennas Wireless Propag. Lett.* **2016**, *15*, 1529.

[22] Y. Shi, S. Fan, *Appl. Phys. Lett.* **2016**, *108*, 021110.

[23] D. L. Sounas, A. Alù, *Nat. Photonics* **2017**, *11*, 774.

[24] M. M. Salary, S. Jafar-Zanjani, H. Mosallaei, *Phys. Rev. B* **2019**, *99*, 045416.

[25] T. J. Cui, M. Q. Qi, X. Wan, J. Zhao, Q. Cheng, *Light: Sci. Appl.* **2014**, *3*, e218.

[26] L. Li, T. J. Cui, W. Ji, S. Liu, J. Ding, X. Wan, Y. B. Li, M. Jiang, C. W. Qiu, S. Zhang, *Nat. Commun.* **2017**, *8*, 197.

[27] L. Li, H. Ruan, C. Liu, Y. Li, Y. Shuang, A. Alù, C.-W. Qiu, T. J. Cui, *Nat. Commun.* **2019**, *10*, 1082.

[28] L. Zhang, S. Liu, L. Li, T. J. Cui, *ACS Appl. Mater. Interfaces* **2017**, *9*, 36447.

[29] S. Liu, L. Zhang, Q. L. Yang, Q. Xu, Y. Yang, A. Noor, Q. Zhang, S. Iqbal, X. Wan, Z. Tian, W. X. Tang, Q. Cheng, J. G. Han, W. L. Zhang, T. J. Cui, *Adv. Opt. Mater.* **2016**, *4*, 1965.

[30] S. Liu, A. Noor, L. L. Du, L. Zhang, Q. Xu, K. Luan, T. Q. Wang, Z. Tian, W. X. Tang, J. G. Han, W. L. Zhang, X. Y. Zhou, Q. Cheng, T. J. Cui, *ACS Photonics* **2016**, *3*, 1968.

[31] L. Zhang, R. Y. Wu, G. D. Bai, H. T. Wu, Q. Ma, X. Q. Chen, T. J. Cui, *Adv. Funct. Mater.* **2018**, *28*, 1802205.

[32] B. Xie, K. Tang, H. Cheng, Z. Liu, S. Chen, J. Tian, *Adv. Mater.* **2017**, *29*, 1603507.

[33] L. Zhang, X. Wan, S. Liu, J. Y. Yin, Q. Zhang, H. T. Wu, T. J. Cui, *IEEE Trans. Antennas Propag.* **2017**, *65*, 3374.

[34] M. Moccia, S. Liu, R. Y. Wu, G. Castaldi, A. Andreone, T. J. Cui, V. Galdi, *Adv. Opt. Mater.* **2017**, 1700455.

[35] T. J. Cui, S. Liu, L. Zhang, *J. Mater. Chem. C* **2017**, *5*, 3644.

[36] S. Liu, T. J. Cui, L. Zhang, Q. Xu, Q. Wang, X. Wan, J. Q. Gu, W. X. Tang, M. Q. Qi, J. G. Han, W. L. Zhang, X. Y. Zhou, Q. Cheng, *Adv. Sci.* **2016**, *3*, 1600156.

[37] J. Zhao, X. Yang, J. Y. Dai, Q. Cheng, X. Li, N. H. Qi, J. C. Ke, G. D. Bai, S. Liu, S. Jin, A. Alù, T. J. Cui, *Natl. Sci. Rev.* **2019**, *6*, 231.

[38] T. J. Cui, S. Liu, G. D. Bai, Q. Ma, *Research* **2019**, 2584509.

[39] J. Y. Dai, W. K. Tang, J. Zhao, X. Li, Q. Cheng, J. C. Ke, M. Z. Chen, S. Jin, T. J. Cui, *Adv. Mater. Technol.* **2019**, *4*, 1900044.

[40] L. Zhang, X. Q. Chen, S. Liu, Q. Zhang, J. Zhao, J. Y. Dai, G. D. Bai, X. Wan, Q. Cheng, G. Castaldi, V. Galdi, T. J. Cui, *Nat. Commun.* **2018**, *9*, 4334.